

Semi-Cycled Generative Adversarial Networks for Real-World Face Super-Resolution

Hao Hou, Xiaotao Hu, Jun Xu, *Member, IEEE*, Yingkun Hou, *Senior Member, IEEE*, Benzhen Wei, and Dinggang Shen, *Fellow, IEEE*

Abstract—Real-world face super-resolution (SR) is a highly ill-posed image restoration task. The fully-cycled Cycle-GAN architecture is widely employed to achieve promising performance on face SR, but prone to produce artifacts upon challenging cases in real-world scenarios, since joint participation in the same degradation branch will impact final performance due to huge domain gap between real-world and synthetic LR ones obtained by generators. To better exploit the powerful generative capability of GAN for real-world face SR, in this paper, we establish two independent degradation branches in the forward and backward cycle-consistent reconstruction processes, respectively, while the two processes share the same restoration branch. Our Semi-Cycled Generative Adversarial Networks (SCGAN) is able to alleviate the adverse effects of the domain gap between the real-world LR face images and the synthetic LR ones, and to achieve accurate and robust face SR performance by the shared restoration branch regularized by both the forward and backward cycle-consistent learning processes. Experiments on two synthetic and two real-world datasets demonstrate that, our SCGAN outperforms the state-of-the-art methods on recovering the face structures/details and quantitative metrics for real-world face SR. The code will be publicly released at <https://github.com/HaoHou-98/SCGAN>.

Index Terms—Real-world face super-resolution, semi-cycled architecture, cycle-consistent generative adversarial networks.

1 INTRODUCTION

FACE is of central importance for human identity recognition. The low-resolution (LR) face images captured by camera sensors would largely degrade the corresponding identity information. Face super-resolution (SR) aims to estimate high-resolution (HR) face images from LR ones, to improve the image quality and performance of subsequent identity recognition tasks [1]–[3]. This task is very challenging upon complex real-world scenarios, where the degradation kernel is usually unknown. Traditional face SR methods can be roughly divided into local patch-based methods [4]–[6], global image-based methods [7]–[9], and hybrid methods taking advantage of global image consistency and local patch sparsity [10]–[13]. However, these hand-crafted methods could hardly achieve satisfactory results upon diverse degradation in real-world scenarios [14].

Recently, the powerful learning capability of deep convolutional neural networks (CNNs) has been extensively exploited for face SR [15]–[19]. These discriminative CNNs mainly learn a direct enhancing mapping function between pairs of LR and HR face images. For objective evaluation,

the LR face images are usually degraded by synthetic downsampling kernels from the HR ones. However, since it is difficult to obtain the corresponding HR face images for the real-world LR ones, the discriminative CNNs suffer from a huge performance gap between synthetic and practical degradation for real-world face SR. To this end, several methods [20]–[22] align LR face images with unpaired HR face images with the same identity. However, face alignment is often challenged by the insufficiently trained face SR models, due to short of HR face images in practical scenarios.

Compared to the discriminative competitors, generative CNNs like Generative Adversarial Networks (GANs) [23] are employed in [14], [20], [24]–[27] to perform blind face SR with complex degradations. To deal with unknown real-world degradation, several generative CNNs [28]–[31] further implement unsupervised face SR by resorting to the insight of cycle-consistency developed for the unpaired image translation tasks [32]. LRGAN [28] is a representative work to utilize the cycle learning scheme [32] for real-world face SR, introducing a “learning-to-degrade” branch and a “learning-to-SR” branch to perform face image degradation and SR, respectively. However, since unpaired LR and HR face images suffer from a considerable gap on identity information, the two branches in LRGAN are consistent only for the HR face images and could hardly preserve well the face details and identity information of the LR face images.

Since the unpaired LR and HR face images suffer from uncertain relationship, employing a directional framework [28] or a fully-cycled bidirectional one [32] is not sufficient to simultaneously preserve the identity information of the LR and HR face images in real-world scenarios. To better alleviate the domain gap between unpaired LR and HR face images, in this paper, we introduce a Semi-Cycled Generative Adversarial Network (SCGAN) for real-world face SR, by

- Corresponding author: Jun Xu (nankaimathxujun@gmail.com)
- H. Hou is with College of Intelligence and Information Engineering, Shandong University of Traditional Chinese Medicine, Ji’nan, 250355, China.
- X.-T. Hu is with College of Computer Science, Nankai University, Tianjin 300071, China.
- J. Xu is with School of Statistics and Data Science, KLMDASR, LEBPS, and LPMC, Nankai University, Tianjin 300071, China, and with School of Biomedical Engineering, ShanghaiTech University, Shanghai, China.
- Y.-K. Hou is with the School of Information Science and Technology, Taishan University, Tai’an, 271000, China.
- B.-Z. Wei and H. Hou are with the Center for Medical Artificial Intelligence, Shandong University of Traditional Chinese Medicine, Ji’nan, 250355, China.
- D.-G. Shen is with School of Biomedical Engineering, ShanghaiTech University, and United Imaging Co., Shanghai, China.



Figure 1. **Comparison of LRGAN [28] and our SCGAN on blind real-world face SR.** We perform $\times 4$ real-world face SR on 16×16 LR face images to obtain 64×64 HR ones. 1-st row: a real-world group photo crawled from the internet that suffers from complex and unknown degradation. 2-nd row: the LR face images from the photo. 3-rd row: the face SR results of LRGAN [28]. 4-th row: the SR results by our SCGAN.

extending the bidirectional cycle consistency scheme in [32] to a more flexible version. Specifically, we propose to learn three generative branches, instead of two in [28], [32], for real-world HR and LR face image reconstructions: 1) a “learning-to-degrade” branch to obtain synthetic LR face images by degrading the HR ones, 2) a “learning-to-SR” branch to obtain the SR images by restoring the synthetic and real-world LR face images, and 3) another “learning-to-degrade” branch to degrade the SR images restored from the real-world LR images. Different from CycleGAN [32], our SCGAN is only coupled at the middle “learning-to-SR” branch, while learning the cycle consistency of LR and HR face image reconstructions by individual branches. For example, in Figure 1, we compare the real-world face SR performance between LRGAN [28] and our SCGAN. The real-world LR face images with severe degradation could hardly be restored by LRGAN to recover the identity structure and details. However, our SCGAN, benefited from the semi-cycle consistency insight, well preserves both aspects for face SR.

In summary, our contributions are mainly three-fold:

- **We develop a novel Semi-Cycled architecture to exploit GANs for real-world face super-resolution.** Our proposed Semi-Cycled GANs (SCGAN) well mitigate adverse effects of the degradation gap between real-world LR face images and synthetic ones, resulting in better preservation of identity and detailed information.
- **We study in-depth the roles of adversarial loss, pixel loss, and cycle-consistency loss** in our SCGAN for face SR. That is, the adversarial loss reduces the domain gap between the HR images and those output by our SCGAN, and the pixel loss enriches the contextual details of the SR results, while the cycle-consistency loss helps to preserve the structural information.
- Experiments on four benchmark datasets show that **our SCGAN outperforms the state-of-the-art methods quantitatively and qualitatively** on real-world face SR.

The following part of this paper is organized as follows. In §2, we summarize the related works. In §3, we introduce our SCGAN for real-world face SR. In §4, experiments on benchmark datasets are conducted to evaluate the performance of different face SR methods. §5 concludes this paper.

2 RELATED WORK

2.1 Human Face Super-Resolution

Human face super-resolution (SR) aims to obtain visual-pleasing high-resolution (HR) face images from the low-resolution ones [33]. Early face SR methods [4]–[6], [34]–[36] utilize hand-craft image priors and degradation models. For instance, Baker *et al.* [34] utilized Gaussian image pyramids for face SR, while Gunturk *et al.* [35] presented a Bayesian model for face SR from a global image-level perspective. To well recover local details, the methods in [4]–[6] tackle the face SR by patch-wise modeling. Neighborhood embedding [6] is a representative work in this direction. Later, the methods of [10]–[13], [36] have been developed for face SR with simultaneous preservation of local details and global structures. However, the above-mentioned methods do not perform well upon complex real-world cases.

Recent methods [15]–[19] employ deep convolutional neural networks (CNNs) for face SR. RBPNet [18] employs iterative back projection to directly learn the mapping from LR to HR face images. SPARNet [17] integrates the spatial attention mechanism into their framework to improve the representation ability of the network. WaSRNet [19] transforms the face image domain into the wavelet coefficient domain to preserve more details. Lu *et al.* [37] proposed a hybrid approach based on a global upsampling network and a local enhancement network to jointly enhance the facial contours and local details. However, since they are trained on synthetic images, these discriminative learning based methods cannot be well generalized to real world scenarios.

Generative models like Generative Adversarial Networks (GANs) [23] have achieved remarkable progress on face SR [28]–[31], [38]. URDGN [39] is among the first work in this direction, but sensitive to the LR face images with large face rotations or poses. To alleviate this problem, Super-FAN [40] locates the key points of faces via heat map regression to deal with faces in different angles and poses, which needs large-scale annotations of face landmarks for model training. LRGAN [28] is an unsupervised face SR network by utilizing the architecture of cycle consistency [32]. But this method only exploits the consistency within the HR face images while ignoring the consistency within the LR ones. PULSE [26] often loses spatial information and identity consistency of face images, by randomly sampling the low-dimensional latent codes. The methods of GLEAN [41], GFPGAN [27] and GPEN [14] utilize a pre-trained StyleGAN [42] model for face SR, but show limited performance on LR face images with severe degradation. In this work, we propose to learn three forward or backward mappings, *i.e.*, two independent “learning-to-degrade” branches and one shared “learning-to-SR” branch, which are semi-cycled to maintain the consistency of both the HR and LR face image reconstructions.

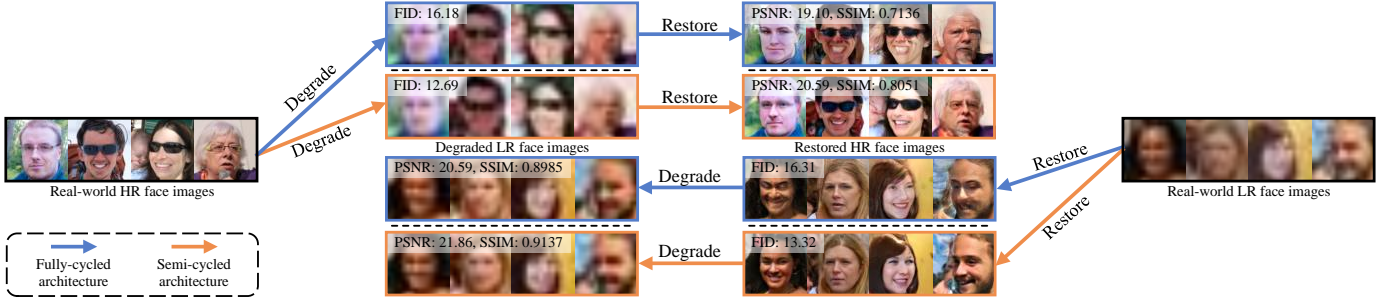


Figure 2. **Comparison of the degradation and restoration results between the fully-cycled CycleGAN architecture [32] and the proposed semi-cycled architecture of SCGAN.** Where the FID (lower is better) is calculated from the degraded LR face image and the real LR face image, and the PSNR and SSIM are calculated from the restored HR face image and the original HR face image. Please zoom in for better view.

2.2 Generative Adversarial Networks

Generative Adversarial Networks (GANs) [23] have been widely utilized in unsupervised computer vision tasks with great success [28]–[32], [38], [43]–[48]. InfoGAN [43] learns explainable feature representation by decomposing the input noise vector into incompressible noise and latent codes, to control semantic features of the generated images. Conditional GAN (cGAN) [44] adds to the original GAN an extra training supervision, achieving great success on image translation tasks [45], [46]. With the insight of cycle consistency, the methods of CycleGAN [32], DualGAN [47], and DiscoGAN [48] achieve promising performance on image translation tasks. This insight has also been resorted by many image restoration methods [28]–[31], [38], [49]. Among them, LRGAN [28] introduces two cycle-consistent generators [32] for face SR: a “learning-to-degrade” branch for HR image degradation and a “learning-to-SR” branch for LR face image super-resolution. However, the two branches are only coupled for HR face image reconstruction, bringing a potential gap between unpaired LR and HR face images. In this work, we also exploit the powerful generative capability of CycleGAN [32] for unsupervised real-world face SR. Built upon LRGAN [28], our SCGAN introduces an additional “learning-to-degrade” branch to degrade the super-resolved face images, which are supervised by the real-world LR ones.

2.3 Cycle-Consistent Learning

The framework of cycle-consistent learning has been developed originally for image-to-image translation [32] to jointly learn a paired of coupled branches under the process of backward domain transfer. From then on, researchers have exploited the cycle-consistent learning framework for many vision tasks such as image restoration [28]–[31], [38]. For example, the methods of [29], [38] simultaneously perform degradation on the LR images and also restoration on the degraded LR images with pseudo-supervision. Guo *et al.* [30] introduced a U-Net like cycle-consistent network for image super-resolution, while Zhang *et al.* [31] employed the cycle-consistent learning for image deblurring. Yi *et al.* [49] proposed an asymmetric cycle-consistent architecture for face portrait line drawing, which is improved by a pre-trained Inception-V3 [50] under a knowledge distillation scheme [51].

Cycle-consistent learning has also been utilized for face SR. LRGAN [28] first learns to degrade the real-world HR face images to the synthetic LR ones by a “learning-to-degrade” sub-network, and then learns to restore the synthetic and real-world LR face images to the corresponding

SR ones by a “learning-to-SR” sub-network. In this paper, we also employ the cycle-consistent learning framework and propose semi-cycled GANs for face SR. Compared to the fully-cycled CycleGAN, our semi-cycled GANs establish independent degradation mappings to alleviate the adverse gap between real-world HR face images and SR ones.

3 PROPOSED METHOD

In this section, we introduce the motivation of our Semi-Cycled Generative Adversarial Networks (SCGAN) for unsupervised face image super-resolution (SR) in §3.1. Then we overview our SCGAN in §3.2. We present three degradation and restoration branches in §3.3, §3.4, and §3.5, respectively. Finally, the implementation details are provided in §3.6.

3.1 Motivation

Our goal is to super-resolve real-world low-resolution (LR) face images into the identity preserving high-resolution (HR) face images, without the corresponding paired real-world HR face images. This task can be suitably tackled under the unsupervised cycle-consistent framework like CycleGAN [32]. With two fully-cycled generators, CycleGAN well preserves the consistency within the bidirectional translation between two different image domains. However, the fully-cycled CycleGAN is prone to get stuck upon real-world unsupervised face SR with unpaired LR and HR face images, since the complex degradation in real-world LR face images can hardly be well simulated by the generator simultaneously synthesizing the HR face degradation. Therefore, directly employing the fully-cycled architecture for real-world face SR inadvertently suffers from an inevitable problem on the degradation gap between synthetic LR images and real-world LR images. To address this problem, it is natural to model the synthetic and real-world degradations by different generators. To this end, our SCGAN is developed with two different degradation branches and one restoration branch to learn semi-cycled forward and backward cycle-consistent reconstruction processes. Our SCGAN is more flexible than the fully-cycled architecture with more accurate unsupervised real-world face SR performance. Besides, the two independent degradation branches in our SCGAN further facilitate our SCGAN to learn a stronger restoration branch for LR face image, making our SCGAN very robust on super-resolving real-world LR face images.

To illustrate this point, we train the fully-cycled CycleGAN and our semi-cycled SCGAN with unpaired HR

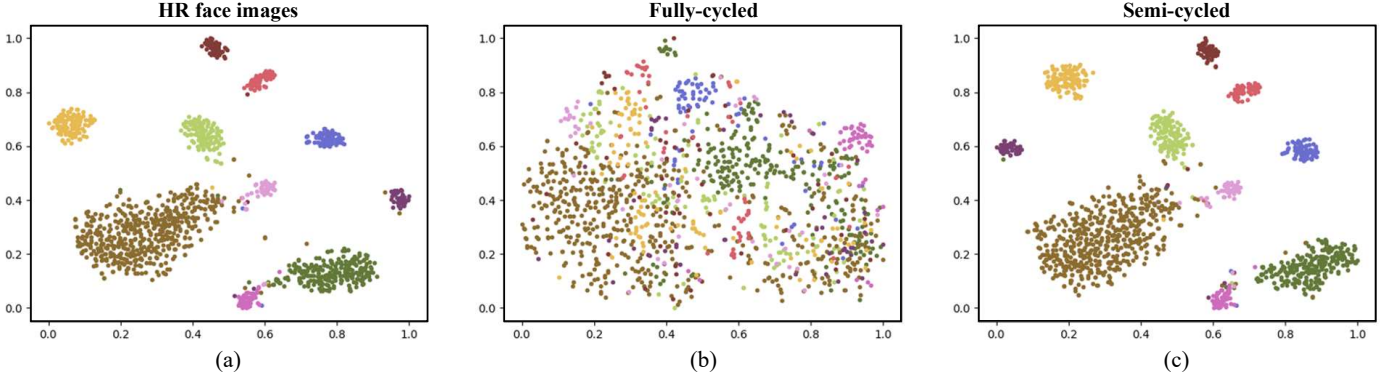


Figure 3. **Distributions of the feature maps extracted by ResNet-101 [52] from HR and SR face images using t-SNE [53].** (a) Visualization of the HR face images. (b) Visualization of the SR face images restored by fully-cycled CycleGAN [32]. (c) Visualization of the SR face images restored by our semi-cycled SCGAN. Our semi-cycled architecture better retains the feature maps of the SR face images compared to the fully-cycled CycleGAN.

face images from the FFHQ dataset [42] and LR ones from the Widerface dataset [54]. To achieve better reconstruction quality, we train the fully-cycled CycleGAN and our semi-cycled SCGAN with an additional pixel-wise loss function, which will be introduced in §3.3. In Figure 2, we first compare the degraded LR images and the restored HR ones by CycleGAN and our SCGAN, respectively, on four typical real-world HR face images. The results of FID scores [55], PSNR, and SSIM [56] are also provided for reference. One can see that the synthetic LR face images degraded from the HR ones in our SCGAN obtains lower FID score than those degraded in the fully-cycled CycleGAN, indicating that our degradation branch obtains more realistic LR face images than those generated by CycleGAN. To evaluate the reconstruction consistency, we also restore the two sets of synthetic LR face images by the corresponding restoration branches in CycleGAN and our SCGAN, respectively. Besides, we compare the restored SR images and the degraded LR ones by CycleGAN and our SCGAN, respectively, on four typical real-world LR face images. We observe that the face images restored by our SCGAN show clear improvement over those restored by CycleGAN on detail recovery. All these results indicate the advantage of our semi-cycled SCGAN over the fully-cycled CycleGAN on unsupervised real-world face SR.

To globally compare our semi-cycled SCGAN with the fully-cycled CycleGAN, we perform degradation and restoration on HR face images of 10 identities from the LFW dataset [57], by the same strategy mentioned above. In Figure 3, we visualize the input HR face images, and the HR face images restored by CycleGAN and our SCGAN via t-SNE [53], using the one-dimensional vectors output by the last fully connected layer of a pre-trained Resnet-101 [52]. One can see that the distribution of HR face images restored by our SCGAN is more consistent than that restored by CycleGAN, compared to the distribution of input HR face images. This validates the superiority of our semi-cycled architecture over the fully-cycled architecture in CycleGAN on the identity preservation of HR face image restoration.

3.2 Network Overview

Our SCGAN contains two semi-cycled sub-networks consisting of two independent degradation branches coupled by a restoration branch. The overall network architecture is

illustrated in Figure 4. The synthetic degradation branch \mathcal{D}_{HL} and the restoration branch \mathcal{R}_{LS} together perform forward cycle-consistent HR face image reconstruction, while the restoration branch \mathcal{R}_{LS} and the real-world degradation branch \mathcal{D}_{SL} together implement the backward cycle-consistent LR face image reconstruction. The two reconstruction sub-networks are semi-cycled to avoid the adverse effect of the domain gap between the synthetic and realistic LR face images, and achieve robust yet accurate face SR performance.

Synthetic HR image degradation branch. The HR face image degradation branch, denoted as \mathcal{D}_{HL} , degrades an HR face image \mathbf{I}_{rH} to a synthetic LR face image. It is the degradation stage of the forward cycle-consistency learning process $\mathbf{I}_{rH} \rightarrow \mathbf{I}_{sL} = \mathcal{D}_{HL}(\mathbf{I}_{rH}) \rightarrow \mathbf{I}_{rH}$, in which the corresponding restoration stage is implemented by the LR face image restoration branch \mathcal{R}_{LS} introduced as follows.

LR face restoration branch. This branch is to enhance the quality of the synthetic LR face image \mathbf{I}_{sL} generated by previous degradation branch \mathcal{D}_{HL} and the real-world LR face image \mathbf{I}_{rL} that is the input in the test stage. The restoration of synthetic LR face image comprises the forward cycle-consistent learning process “ $\mathbf{I}_{rH} \rightarrow \mathcal{D}_{HL}(\mathbf{I}_{rH}) \rightarrow \mathcal{R}_{LS}(\mathcal{D}_{HL}(\mathbf{I}_{rH}))$ ”, together with the previous synthetic degradation branch, and simultaneously comprises the backward cycle-consistency learning process “ $\mathbf{I}_{rL} \rightarrow \mathcal{R}_{LS}(\mathbf{I}_{rL}) \rightarrow \mathcal{D}_{SL}(\mathcal{R}_{LS}(\mathbf{I}_{rL}))$ ”, in which the corresponding degradation stage is implemented by the real-world HR face image degradation branch \mathcal{D}_{SL} introduced as follows.

Real-world HR face degradation branch. Since the real-world and synthetic LR face images suffer from an inevitable degradation gap, it is reasonable to separately degrade the real-world HR face image \mathbf{I}_{rH} and the synthetic one \mathbf{I}_{sH} generated from the restoration branch \mathcal{R}_{LH} by respective branches. The real-world HR face degradation branch, with the restoration one, comprise the backward cycle-consistent learning process “ $\mathbf{I}_{rL} \rightarrow \mathcal{R}_{LH}(\mathbf{I}_{rL}) \rightarrow \mathcal{D}_{SL}(\mathcal{R}_{LH}(\mathbf{I}_{rL}))$ ”.

3.3 Synthetic Degradation Branch on HR Face Image

This branch, denoted as \mathcal{D}_{HL} , aims to learn the degradation process from real-world HR face images to synthetic LR ones. Given a real-world HR face image $\mathbf{I}_{rH} \in \mathbb{R}^{H \times W \times 3}$, we randomly generate a noise vector $\mathbf{z} \in \mathbb{R}^{HW}$, reshape it into the size of $H \times W$, and concatenate it with \mathbf{I}_{rH} along

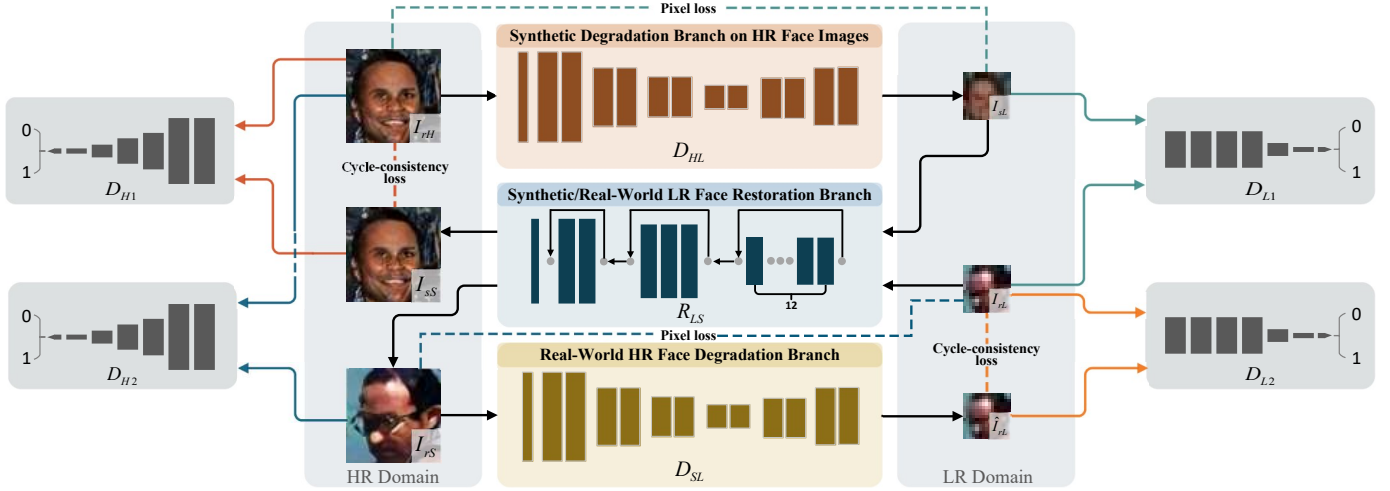


Figure 4. **Architecture of our Semi-Cycled Generative Adversarial Network (SCGAN) for unsupervised face super resolution.** Given a real-world HR face image \mathbf{I}_{rH} , we first perform image degradation through the HR face degradation branch \mathcal{D}_{HL} and compute the pixel loss between the downsampled \mathbf{I}_{rH} and the obtained \mathbf{I}_{sL} to preserve more details. Then \mathbf{I}_{sL} is sent to the sub-network \mathcal{R}_{LS} to perform SR to obtain \mathbf{I}_{sS} . Here, we calculate the cycle consistency loss for \mathbf{I}_{rH} and \mathbf{I}_{sS} to maintain their identity consistency. The above process forms a forward cycle consistent GAN model. Among them, \mathcal{D}_{L1} is responsible for distinguishing \mathbf{I}_{sL} and unpaired input LR face image \mathbf{I}_{rL} , \mathcal{D}_{H1} is responsible for distinguishing \mathbf{I}_{rH} and paired SR result \mathbf{I}_{sS} . The backward cycle consistent GAN model is similar to the forward one. The most important difference with CycleGAN [32] is that, the backward model has an independent degradation sub-network \mathcal{D}_{SL} , while not in the fully-cycled situation.

the channel dimension. This is to simulate different degrees and types of noise contained in real-world LR face images, as suggested in [44]. The concatenated tensor $[\mathbf{I}_{rH}, \mathbf{z}] \in \mathbb{R}^{H \times W \times 4}$ is then fed into the degradation branch \mathcal{D}_{HL} to produce a synthetic LR face image \mathbf{I}_{sL} :

$$\mathbf{I}_{sL} = \mathcal{D}_{HL}([\mathbf{I}_{rH}, \mathbf{z}], \Theta_{HL}), \quad (1)$$

where Θ_{HL} is the set of learnable parameters for \mathcal{D}_{HL} .

As shown in Figure 5 (a), the synthetic degradation branch \mathcal{D}_{HL} is in an encoder-decoder architecture. The encoder begins with a Spectral Normalization (SN) [58], followed by a 3×3 convolutional layer (conv.) and a global average pooling (GAP). Then six residual blocks (Resblocks) are used to extract meaningful feature. As shown in Figure 5 (d), the ResBlock used in \mathcal{D}_{HL} contains two successive sets of SN, ReLU, and 3×3 conv., with a skip connection for feature addition. Here, we use SN to mitigate unstable model training and gradient explosion with the 1-Lipschitz constraint, as suggested in [58]. GAP is used after every two ResBlocks to reduce feature resolution by a factor of 2. The decoder also has six Resblocks, with two Pixel-Shuffle operations used after the second and fourth ResBlocks to upsample feature resolution by a factor of 2. Finally, this branch has two groups of Resblock and 3×3 Conv., followed by a ReLU or a Tanh function for nonlinear activation, respectively, and outputs the degraded LR face image \mathbf{I}_{sL} .

To approximate the degradation in real-world LR face images, the synthetic degradation branch \mathcal{D}_{HL} is learned with an adversarial loss function and a pixel loss function as:

$$l_{\mathcal{D}_{HL}} = \alpha l_{adv}^{\mathcal{D}_{L1}} + \beta l_{pix}^{\mathbf{I}_{sL}}, \quad (2)$$

where α and β are the weights of the two loss functions.

Adversarial loss $l_{adv}^{\mathcal{D}_{L1}}$ uses a discriminator \mathcal{D}_{L1} to predict the real-world LR face image \mathbf{I}_{rL} as 1 and the synthetic LR one \mathbf{I}_{sL} as 0, respectively. As shown in Figure 5 (c), the discriminator \mathcal{D}_{L1} contains six Resblocks followed by a fully connected layer. The max-pooling is used before the last two

Resblocks to reduce the resolution of the feature map. Similar to [58], we use the hinge loss as follows,

$$l_{adv}^{\mathcal{D}_{L1}} = \mathbb{E}_{\mathbf{I}_{rL} \sim \mathbf{P}_{rL}} [\min(0, \mathcal{D}_{L1}(\mathbf{I}_{rL}) - 1)] + \mathbb{E}_{\mathbf{I}_{sL} \sim \mathbf{P}_{sL}} [\min(0, -1 - \mathcal{D}_{L1}(\mathbf{I}_{sL}))], \quad (3)$$

where \mathbf{P}_{rL} and \mathbf{P}_{sL} are the distributions of real-world LR face image \mathbf{I}_{rL} and the synthetic one \mathbf{I}_{sL} degraded by \mathcal{D}_{HL} from the real-world HR face image \mathbf{I}_{rH} , respectively.

Pixel loss $l_{pix}^{\mathbf{I}_{sL}}$ is calculated between the synthetic degradation image \mathbf{I}_{sL} and the input HR face image \mathbf{I}_{rH} downsampled to the same resolution with \mathbf{I}_{sL} by average pooling. Here, we adopt the ℓ_1 loss function that is widely used in image SR task [28], [59] to well recover image details.

3.4 Synthetic/Real-World LR Face Restoration Branch

The LR face restoration branch \mathcal{R}_{LS} is a hub shared by the forward and backward cycle-consistency learning processes. In the forward learning process, it restores the synthetic LR image \mathbf{I}_{sL} degraded from the HR face image \mathbf{I}_{rH} via \mathcal{D}_{HL} , while in the backward learning process, it restores the real-world LR face image \mathbf{I}_{rL} . Denote the SR image restored from \mathbf{I}_{sL} as \mathbf{I}_{sS} and the SR image restored from \mathbf{I}_{rL} as \mathbf{I}_{rS} , the restoration process is as follows:

$$\mathbf{I}_{sS} = \mathcal{R}_{LS}(\mathbf{I}_{sL}, \Theta_{LS}), \quad (4)$$

$$\mathbf{I}_{rS} = \mathcal{R}_{LS}(\mathbf{I}_{rL}, \Theta_{LS}), \quad (5)$$

where Θ_{LS} is the learnable parameters of the branch \mathcal{R}_{LS} .

As shown in Figure 5 (b), our restoration branch \mathcal{R}_{LS} also begins with a Spectral Normalization [58], followed by a 3×3 convolutional layers. Then three groups of 12, 3, and 2 Resblocks are used to extract meaningful features, and in each group the input and output of each group have a skip connection for feature addition to preserve high-frequency details. To enhance its resolution, the feature map is upsampled by a factor of 4 by two bilinear interpolations, followed by a group of "ReLU-Resblock- 3×3 Conv." and a

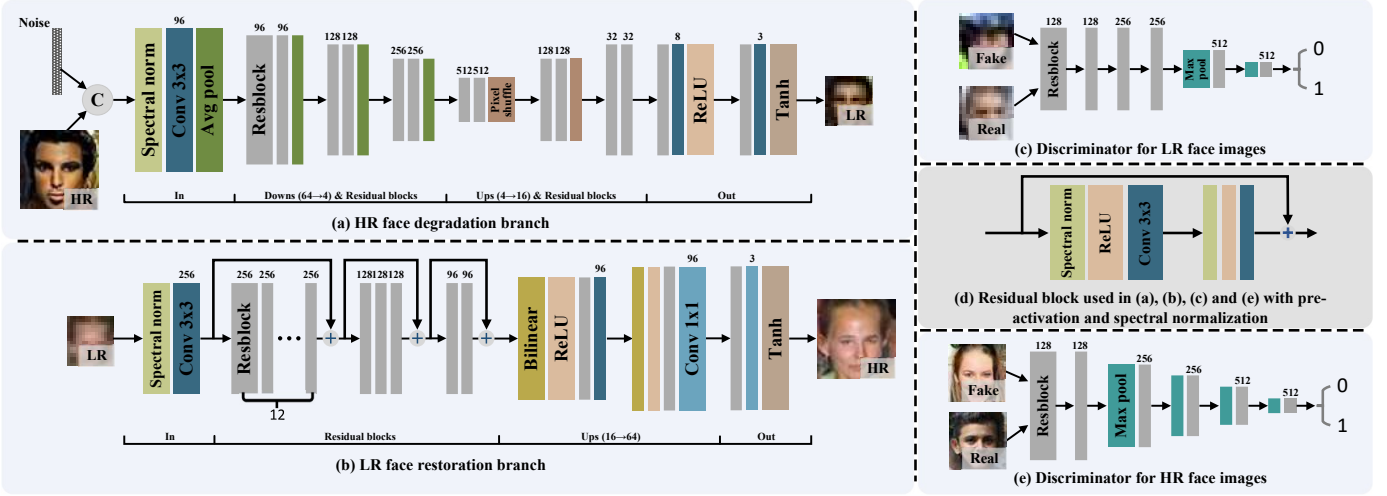


Figure 5. Architectures of the synthetic and real-world HR face degradation branches \mathcal{D}_{HL} and \mathcal{D}_{SL} (a), and the LR face restoration branch \mathcal{D}_{LS} (b). The discriminators are shown in (c) and (e). The residual block used in them is shown in (d). Please zoom in for the best view.

group of “ReLU-Resblock- 1×1 Conv.”, respectively. Finally, this branch outputs the restored HR face image through a Resblock, a 1×1 Conv., and a Tanh activation function.

The restoration branch \mathcal{R}_{LS} aims to generate high-quality SR face images, shared by the forward and backward learning processes. For the loss function, we use the combination of adversarial loss $l_{adv}^{\mathcal{D}_{H1}}$ and the cycle-consistency loss $l_{cyc}^{\mathcal{I}_{SS}}$ in the forward learning process, and use the combination of adversarial loss $l_{adv}^{\mathcal{D}_{H2}}$ and pixel loss $l_{pix}^{\mathcal{I}_{rS}}$ in the backward learning process. The overall loss function for this branch is

$$l_{\mathcal{R}_{LS}} = \theta l_{\mathcal{R}_{LS}}^{\mathcal{I}_{SS}} + \gamma l_{\mathcal{R}_{LS}}^{\mathcal{I}_{rS}}, \quad (6)$$

where θ and γ are the corresponding weights, and

$$l_{\mathcal{R}_{LS}}^{\mathcal{I}_{SS}} = \alpha l_{adv}^{\mathcal{D}_{H1}} + \beta l_{cyc}^{\mathcal{I}_{SS}}, \quad (7)$$

$$l_{\mathcal{R}_{LS}}^{\mathcal{I}_{rS}} = \alpha l_{adv}^{\mathcal{D}_{H2}} + \beta l_{pix}^{\mathcal{I}_{rS}}. \quad (8)$$

Adversarial loss. We use a discriminator \mathcal{D}_{H1} to predict the real-world HR face image I_{rH} as 1 and the synthetic SR image I_{sS} as 0, respectively. Similarly, we use a discriminator \mathcal{D}_{H2} to predict the real-world HR face image I_{rH} as 1 and the real-world SR image I_{rS} as 0, respectively. The adversarial losses $l_{adv}^{\mathcal{D}_{H1}}$ and $l_{adv}^{\mathcal{D}_{H2}}$ are computed as follows,

$$l_{adv}^{\mathcal{D}_{H1}} = \mathbb{E}_{I_{rH} \sim \mathbf{P}_{rH}} [\min(0, \mathcal{D}_{H1}(I_{rH}) - 1)] + \mathbb{E}_{I_{sS} \sim \mathbf{P}_{sS}} [\min(0, -1 - \mathcal{D}_{H1}(I_{sS}))], \quad (9)$$

$$l_{adv}^{\mathcal{D}_{H2}} = \mathbb{E}_{I_{rH} \sim \mathbf{P}_{rH}} [\min(0, \mathcal{D}_{H2}(I_{rH}) - 1)] + \mathbb{E}_{I_{rS} \sim \mathbf{P}_{rS}} [\min(0, -1 - \mathcal{D}_{H2}(I_{rS}))]. \quad (10)$$

Here, \mathbf{P}_{rH} , \mathbf{P}_{sS} , and \mathbf{P}_{rS} are the distributions of real-world HR face image \mathbf{I}_{rH} , synthetic SR image \mathbf{I}_{sS} restored by \mathcal{R}_{LS} from the synthetic LR face image \mathbf{I}_{sL} , and real-world SR image \mathbf{I}_{rS} restored by \mathcal{R}_{LS} from the real-world LR face image \mathbf{I}_{rL} , respectively. The discriminators \mathcal{D}_{H1} and \mathcal{D}_{H2} are in the same structure, which contains six Resblocks followed by a fully connected layer and uses max-pooling before the last four Resblocks, as shown in Figure 5 (e).

Cycle-consistency loss $l_{cyc}^{\mathcal{I}_{SS}}$ is an ℓ_1 loss function used here to make our restoration branch \mathcal{R}_{LS} well preserve the identity information and well recover the face details.

Pixel loss $l_{pix}^{\mathcal{I}_{rS}}$ is an ℓ_1 loss function to penalize the difference between real-world HR face image \mathbf{I}_{rH} and SR one \mathbf{I}_{rL} (upsampled to the same size of \mathbf{I}_{rH} by bicubic interpolation).

3.5 Real-World HR Face Degradation Branch

This branch, denoted as \mathcal{D}_{SL} , learns to degrade the real-world SR face image \mathbf{I}_{rS} restored from the real-world LR image \mathbf{I}_{rL} via \mathcal{R}_{SL} as follows,

$$\hat{\mathbf{I}}_{rL} = \mathcal{D}_{SL}(\mathbf{I}_{rS}; \Theta_{SL}), \quad (11)$$

where Θ_{SL} is the learnable parameters. As shown in Figure 5 (b), the architecture of \mathcal{D}_{SL} is the same as that of the synthetic HR face degradation branch \mathcal{D}_{HL} introduced in §3.3.

To make the branch \mathcal{D}_{SL} generate degradation results that are close to real-world LR face images, here, we employ the adversarial loss $l_{adv}^{\mathcal{D}_{L2}}$ and the cycle-consistency loss $l_{cyc}^{\hat{\mathbf{I}}_{rL}}$ between the output LR image $\hat{\mathbf{I}}_{rL}$ and the real-world one \mathbf{I}_{rL} , which are computed as follows,

$$l_{\mathcal{D}_{SL}} = \alpha l_{adv}^{\mathcal{D}_{L2}} + \beta l_{cyc}^{\hat{\mathbf{I}}_{rL}}. \quad (12)$$

Adversarial loss $l_{adv}^{\mathcal{D}_{L2}}$ uses a discriminator \mathcal{D}_{L2} to predict the real-world LR face image \mathbf{I}_{rL} as 1 and the output LR one $\hat{\mathbf{I}}_{rL}$ as 0, respectively. The architecture of \mathcal{D}_{L2} is the same as that of \mathcal{D}_{L1} introduced in §3.3. Similar to Eq. (3), the adversarial loss $l_{adv}^{\mathcal{D}_{L2}}$ is computed as follows,

$$l_{adv}^{\mathcal{D}_{L2}} = \mathbb{E}_{\mathbf{I}_{rL} \sim \mathbf{P}_{rL}} [\min(0, \mathcal{D}_{L2}(\mathbf{I}_{rL}) - 1)] + \mathbb{E}_{\hat{\mathbf{I}}_{rL} \sim \mathbf{P}_{\hat{rL}}} [\min(0, -1 - \mathcal{D}_{L2}(\hat{\mathbf{I}}_{rL}))], \quad (13)$$

where \mathbf{P}_{rL} and $\mathbf{P}_{\hat{rL}}$ are the distributions of real-world LR face image \mathbf{I}_{rL} and synthetic one $\hat{\mathbf{I}}_{rL}$ degraded by \mathcal{D}_{SL} from the real-world SR face image \mathbf{I}_{rS} , respectively.

Cycle-consistency loss $l_{cyc}^{\hat{\mathbf{I}}_{rL}}$ is an ℓ_1 loss function to penalize the difference between the LR image $\hat{\mathbf{I}}_{rL}$ degraded by this branch and the corresponding real-world LR face image \mathbf{I}_{rL} .

3.6 Implementation Details

The parameters of all three branches in our SCGAN are initialized by Kaiming initialization [60], and optimized by

Adam [61] with $\beta_1 = 0.9$ and $\beta_2 = 0.999$. We set $\alpha = 1$, $\beta = 0.05$ in Eqs. (2)-(8) and $\theta = 1$, $\gamma = 0.05$ in Eq. (6). Our SCGAN is trained for 200 epochs. The learning rate is initialized as 1×10^{-4} and decayed to 1×10^{-5} with the cosine annealing scheme at every 10 epochs. The batch size is set as 64. We implement our SCGAN in PyTorch [62] and train it on a Tesla V100 GPU, which takes about 42 hours.

4 EXPERIMENTS

In this section, we first introduce the experimental setup, including the dataset and evaluation metrics in §4.1. We then conduct a comprehensive ablation study in §4.2 to validate the role of each component of our SCGAN on face SR. Comparison with the state-of-the-art methods on real-world face SR are presented in §4.3. Finally, we apply our SCGAN into three other vision tasks, *e.g.*, face detection, face verification, and face landmark detection in §4.4.

4.1 Dataset and Evaluation Metric

Training set. We train our SCGAN, its variants (to be introduced in §4.2), and all the comparison methods (to be introduced in §4.3) with the 20,000 high-quality, high-resolution (HR) face images from the real-world FFHQ dataset [42] and the 4,000 low-quality, low-resolution (LR) face images from the real-world Widerface dataset [54].

Test set. We evaluate the comparison methods on four popular face SR datasets, including two synthetic datasets, *i.e.*, *LS3D-W balanced* [63] and *FFHQ* [42], and two real-world datasets, *i.e.*, *Widerface* [54] and our newly collected *Webface*:

- *LS3D-W balanced* [63] contains 7,200 HR face images taken in different scenes and poses. We randomly select 1000 face images and perform simple bilinear downsampling to produce synthetic LR face images.
- *FFHQ* [42] contains 70,000 HR face images, 20,000 of which are used as the training set. We randomly select 2,500 images from the remaining images to perform random degradation $I_{sL} = ((I_{rL} \otimes k) \downarrow + n_\delta)_{JPEG_q}$ to produce the synthetic LR face images, as suggested in [28]. Here, k is a Gaussian blur kernel, \downarrow is a downsampling operation randomly chose from bilinear or bicubic at a scaling factor of 4, n_δ is additive white Gaussian noise, and $JPEG_q$ is the JPEG compression with quality factor q . For each degradation, we randomly sample $k \in [0.5, 8]$, $\delta \in [1, 25]$, and $q \in [30, 95]$, respectively.
- *Widerface* [54] contains 32,203 real-world LR face images from 62 versatile scenes, and we randomly select 2,000 images with unknown yet complex degradation process.
- *WebFace*. We crawled 1,028 real-world LR face images, with different genders, ages, races, expression, postures, and unknown degradation process, from the internet.

Evaluation metrics. We employ feature-level and image-level metrics to objectively and comprehensively evaluate results of different methods. On all test sets, we use the Fréchet Inception Distance (FID) [55] and Kernel Inception Distance (KID) [64] to evaluate the distribution distance between the output SR images and real-world HR face images on diversity and visual quality, respectively. On two synthetic test sets, we also use the Learned Perceptual Image Patch Similarity (LPIPS) [65] to measure the distance of human perception

Table 1
Quantitative results on two synthetic and two real-world datasets by our SCGAN and its variants with different architectures. The best, second best, and third best results are highlighted in **red**, **blue** and **bold**, respectively.

Dataset	Variant	FID ↓	KID ↓	LPIPS ↓
LS3D-W balanced [68]	SCGAN-w/o- \mathcal{D}_{SL}	43.24	3.64±0.10	0.081
	SCGAN-w/o- \mathcal{D}_{HL}	27.49	3.51±0.10	0.129
	SCGAN-fc	25.84	1.99±0.07	0.088
	SCGAN	22.55	1.26±0.06	0.068
FFHQ [42]	SCGAN-w/o- \mathcal{D}_{SL}	27.57	3.18±0.09	0.242
	SCGAN-w/o- \mathcal{D}_{HL}	19.25	3.44±0.12	0.310
	SCGAN-fc	15.15	2.00±0.08	0.247
	SCGAN	9.06	0.94±0.05	0.197
Dataset	Variant	FID ↓	KID ↓	NIQE ↓
Widerface [54]	SCGAN-w/o- \mathcal{D}_{SL}	33.96	3.14±0.11	6.5738
	SCGAN-w/o- \mathcal{D}_{HL}	20.53	3.36±0.12	6.7653
	SCGAN-fc	16.02	1.65±0.06	6.7538
	SCGAN	13.32	1.08±0.05	6.6192
WebFace	SCGAN-w/o- \mathcal{D}_{SL}	40.57	3.75±0.10	6.5697
	SCGAN-w/o- \mathcal{D}_{HL}	25.29	3.32±0.10	6.7358
	SCGAN-fc	23.31	2.10±0.07	6.7464
	SCGAN	21.06	1.39±0.06	6.5835

between the SR images and the corresponding ground-truth ones. On two real-world test sets, we also use the widely used Natural Image Quality Evaluator (NIQE) [66] to evaluate the naturalness of restored face images. Besides, we compute the detection accuracy of the method based on Histogram of Oriented Gradient and Support Vector Machine [67] on the SR face images from each dataset, which indirectly measures the capability of face SR methods on identity preservation.

4.2 Ablation Study

To study the role of each component in our SCGAN to its effectiveness on real-world face SR, here, we conduct detailed examinations of our SCGAN on different LR face image test sets. Specifically, we access a) the benefits of our semi-cycle architecture; b) whether to share parameters of two degradation branches or not in our SCGAN; c) how different loss functions (adversarial loss, pixel loss, and cycle consistency loss) contribute to our SCGAN; d) how different combinations of adversarial losses influence our SCGAN.

a) How the semi-cycled architecture benefits our SCGAN on real-world face SR? To answer this question, we develop three variants of our SCGAN. 1) We remove the real-world HR face degradation branch \mathcal{D}_{SL} introduced in §3.5, and only train the forward cycle-consistency reconstruction process " $\mathcal{D}_{HL} \rightarrow \mathcal{R}_{LS}$ ". This variant is denoted as "SCGAN-w/o- \mathcal{D}_{SL} ". 2) We remove the synthetic degradation branch \mathcal{D}_{HL} introduced in §3.3, and only train the backward cycle-consistency reconstruction process " $\mathcal{R}_{LS} \rightarrow \mathcal{D}_{SL}$ ". This variant is denoted as "SCGAN-w/o- \mathcal{D}_{HL} ". 3) We share the parameters of synthetic HR face degradation branch \mathcal{D}_{HL} and real-world one \mathcal{D}_{SL} , and jointly train the forward cycle-consistency reconstruction process $\mathcal{D}_{HL} \rightarrow \mathcal{R}_{LS}$ as well as the backward one $\mathcal{R}_{LS} \rightarrow \mathcal{D}_{SL}$. This variant is denoted as "SCGAN-fc". The quantitative results are listed in Table 1. We observe that our SCGAN achieves better results in term of FID, KID, and LPIPS, with comparable NIQE results, than

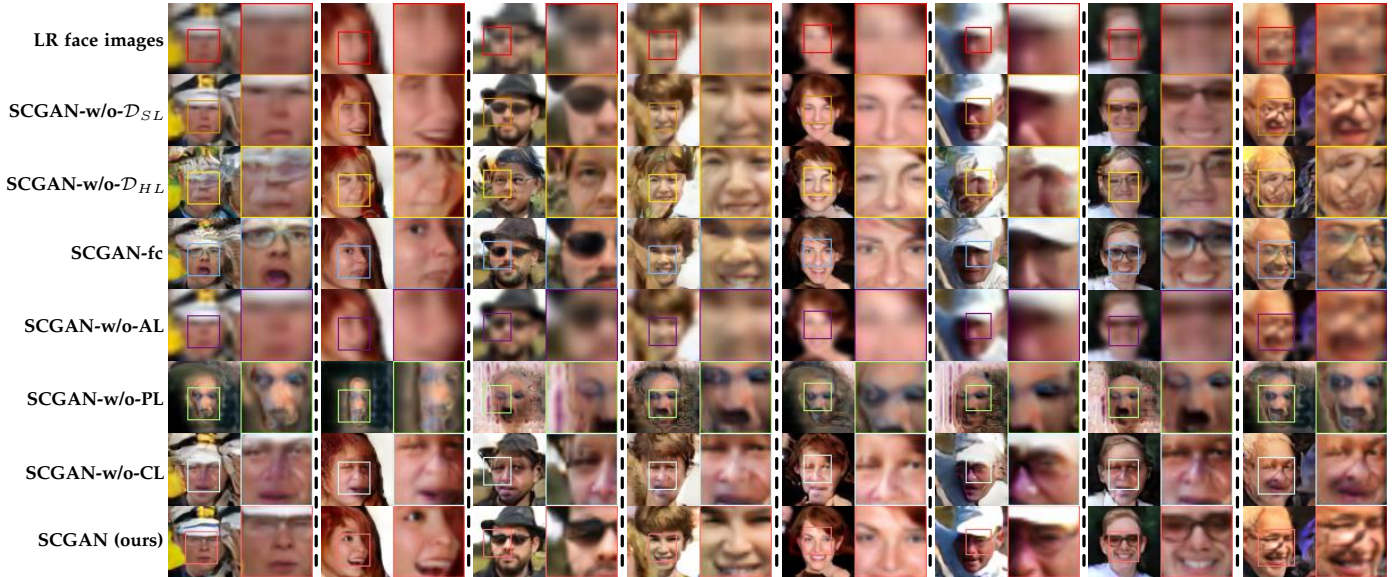


Figure 6. Comparison results by different variants of our SCGAN on representative LR face images from the Widerface [54] dataset.

Table 2

Quantitative results on two synthetic and two real-world datasets by our SCGAN and its variants with different parameter-sharing schemes in two degradation branches. The best, second best, and third best results are highlighted in **red**, **blue** and **bold**, respectively.

Dataset	Variant	FID ↓	KID ↓	LPIPS ↓
LS3D-W balanced [68]	SCGAN-SA	25.54	2.10±0.10	0.073
	SCGAN-SE	23.47	2.19±0.08	0.073
	SCGAN-SD	23.33	1.39±0.08	0.068
	SCGAN-SM	23.12	1.28±0.06	0.077
	SCGAN	22.55	1.26±0.06	0.068
FFHQ [42]	SCGAN-SA	10.65	1.05±0.05	0.200
	SCGAN-SE	10.59	1.64±0.07	0.209
	SCGAN-SD	10.96	1.11±0.06	0.198
	SCGAN-SM	11.57	1.31±0.07	0.219
	SCGAN	9.06	0.94±0.05	0.197
Dataset	Variant	FID ↓	KID ↓	NIQE ↓
Widerface [54]	SCGAN-SA	15.36	1.45±0.08	6.6553
	SCGAN-SE	14.30	1.64±0.09	6.6534
	SCGAN-SD	13.61	1.11±0.05	6.6741
	SCGAN-SM	14.58	1.23±0.07	6.7038
	SCGAN	13.32	1.08±0.05	6.6192
WebFace	SCGAN-SA	21.77	1.86±0.08	6.6563
	SCGAN-SE	22.04	2.14±0.08	6.5968
	SCGAN-SD	21.49	1.43±0.07	6.6875
	SCGAN-SM	21.69	1.70±0.07	6.7028
	SCGAN	21.06	1.39±0.06	6.5835

the other variants. This demonstrates that our semi-cycled architecture really benefits the real-world face SR task.

b) Whether to share parameters or not in the two degradation branches in our SCGAN? Here, we study whether to share parameters or not in the two degradation branches \mathcal{D}_{HL} and \mathcal{D}_{SL} of our semi-cycled SCGAN. To this end, we design four other variants of our SCGAN with degradation branches \mathcal{D}_{HL} sharing partial parameters (except for the input head and output head). 1) We share the parameters of all layers except the input and output heads (denoted as “In” and “Out” in Figure 5) in \mathcal{D}_{HL} and \mathcal{D}_{SL} , and denote

Table 3

Quantitative results on two synthetic and two real-world datasets by our SCGAN and its variants with different loss functions. The best, second best, and third best results are highlighted in **red**, **blue** and **bold**, respectively.

Dataset	Variant	FID ↓	KID ↓	LPIPS ↓
LS3D-W balanced [68]	SCGAN-w/o-AL	235.60	10.47±0.10	0.343
	SCGAN-w/o-PL	185.45	24.48±0.24	0.360
	SCGAN-w/o-CL	33.62	4.11±0.09	0.117
	SCGAN	22.55	1.26±0.06	0.068
FFHQ [42]	SCGAN-w/o-AL	235.76	11.81±0.18	0.916
	SCGAN-w/o-PL	181.00	24.89±0.35	0.877
	SCGAN-w/o-CL	24.29	4.21±0.12	0.289
	SCGAN	9.06	0.94±0.05	0.197
Dataset	Variant	FID ↓	KID ↓	NIQE ↓
Widerface [54]	SCGAN-w/o-AL	233.94	11.00±0.16	7.7086
	SCGAN-w/o-PL	186.03	24.88±0.30	6.8927
	SCGAN-w/o-CL	26.49	4.21±0.12	6.7678
	SCGAN	13.32	1.08±0.05	6.6192
WebFace	SCGAN-w/o-AL	239.39	12.49±0.12	7.7209
	SCGAN-w/o-PL	189.44	24.55±0.26	6.9038
	SCGAN-w/o-CL	31.68	4.48±0.10	6.7251
	SCGAN	21.06	1.39±0.06	6.5835

this variant as “SCGAN-SA”. 2) We share the parameters of the encoder layers in \mathcal{D}_{HL} and \mathcal{D}_{SL} , and denote this variant as “SCGAN-SE”. 3) We share the parameters of the decoder layers in \mathcal{D}_{HL} and \mathcal{D}_{SL} , and denote this variant as “SCGAN-SD”. 4) We share the parameters of the middle part, *i.e.*, the last two groups of Resblocks in the encoder and the first two groups in the decoder, in \mathcal{D}_{HL} and \mathcal{D}_{SL} . We denote this variant as “SCGAN-SM”. The objective results are listed in Table 2. One can see that our SCGAN with two independent degradation branch achieves the best results among all these variants in terms of all four objective metrics.

c) How different loss functions (*i.e.*, adversarial loss, pixel loss and cycle consistency loss) contribute to our SCGAN on face SR? We design three variants of our SCGAN to better understand the role of different loss functions: 1) We

Table 4
Quantitative results on two real-world LR face image datasets by our SCGAN and its 15 more variants with different combinations of adversarial losses. The best, second best, and third best results are highlighted in **red**, **blue** and **bold**, respectively.

Removal number	Variant	$l_{adv}^{\mathcal{D}_{L1}}$	$l_{adv}^{\mathcal{D}_{L2}}$	$l_{adv}^{\mathcal{D}_{H1}}$	$l_{adv}^{\mathcal{D}_{H2}}$	Widerface [54]			WebFace		
						FID ↓	KID ↓	NIQE ↓	FID ↓	KID ↓	NIQE ↓
4	l_{adv} -4-1	✗	✗	✗	✗	233.94	11.00±0.16	7.7086	239.39	12.49±0.12	7.7209
3	l_{adv} -3-1	✗	✗	✗	✓	31.68	3.31±0.11	6.7656	41.60	4.07±0.11	6.7961
	l_{adv} -3-2	✗	✗	✓	✗	222.02	9.55±0.15	7.0507	228.72	10.94±0.12	7.0907
	l_{adv} -3-3	✗	✓	✗	✗	230.46	10.40±0.15	7.1812	236.07	11.86±0.12	7.2225
	l_{adv} -3-4	✓	✗	✗	✗	98.33	4.98±0.12	6.8866	108.11	5.65±0.11	6.8991
2	l_{adv} -2-1	✗	✗	✓	✓	14.00	1.09±0.05	6.6933	21.51	1.50±0.06	6.6727
	l_{adv} -2-2	✗	✓	✗	✓	201.45	8.60±0.14	6.9884	207.31	9.81±0.11	7.0166
	l_{adv} -2-3	✗	✓	✓	✗	213.81	9.15±0.14	7.0584	220.66	10.23±0.11	7.0915
	l_{adv} -2-4	✓	✗	✗	✓	34.27	4.12±0.12	6.8002	43.71	4.75±0.12	6.8045
	l_{adv} -2-5	✓	✗	✓	✗	215.76	9.65±0.14	7.0541	222.01	10.29±0.11	7.1055
	l_{adv} -2-6	✓	✓	✗	✗	233.59	10.94±0.16	7.2024	238.47	12.29±0.12	7.2139
1	l_{adv} -1-1	✗	✓	✓	✓	17.44	1.52±0.07	6.7663	24.46	1.85±0.08	6.7707
	l_{adv} -1-2	✓	✗	✓	✓	231.55	10.97±0.16	7.0690	236.46	12.42±0.13	7.0960
	l_{adv} -1-3	✓	✓	✗	✓	36.59	4.53±0.12	6.8268	46.41	5.09±0.12	6.8242
	l_{adv} -1-4	✓	✓	✓	✗	208.74	8.77±0.13	7.0242	217.33	9.66±0.11	7.0768
0	SCGAN	✓	✓	✓	✓	13.32	1.08±0.05	6.6192	21.06	1.39±0.06	6.5835

remove all adversarial losses in our SCGAN, and denote this variant as “SCGAN-w/o-AL”; 2) We remove all pixel losses in our SCGAN, and denote this variant as “SCGAN-w/o-PL”; 3) We remove all cycle-consistency losses in our SCGAN, and denote this variant as “SCGAN-w/o-CL”. The results of FID, KID and NIQE listed in Table 3 show that our SCGAN without either loss function achieves inferior performance to the original SCGAN. The visual comparison results on Widerface [54] are shown in Figure 6. We observe that the variant “SCGAN-w/o-AL” fails to recover well the face details, and the variant “SCGAN-w/o-PL” could not guarantee the contextual consistency with the input real-world LR face images, while the variant “SCGAN-w/o-CL” hard to preserve structural consistency on identity. On the contrary, by integrating all three loss functions, our SCGAN recovers well the contextual and detailed information to preserve the face identity. These demonstrates that the adversarial loss is mainly used to recover face details, and the pixel loss is mainly used to preserve the contextual information, while the cycle-consistency loss is mainly used to keep the structural identity consistency.

d) How different combinations of adversarial losses influence our SCGAN? Our SCGAN has 4 adversarial losses. To study this problem, we design 15 more variants of our SCGAN in 4 categories, according to the number of removed adversarial losses. The variants are denoted as “ l_{adv} -a-b”, where “a” represents the number of removed adversarial losses, and “b” represents the possible combination of the remaining 4-a adversarial losses. The details of the variants and the objective results are summarized in Table 4. We have four main observations: 1) With all the 4 adversarial losses, our SCGAN achieves better results than the other 15 variants. This demonstrates the essential role of every adversarial loss in our SCGAN for promising face SR performance. 2) By removing one adversarial loss, our SCGAN without \mathcal{D}_{L2} or \mathcal{D}_{H2} degrades greatly in terms of all four evaluation metrics. This reveals the dominate role of the adversarial losses in the backward cycle-consistency learning process

for effective real-world LR face restoration. 3) By removing two adversarial losses, our SCGAN without \mathcal{D}_{L1} and \mathcal{D}_{L2} (“ l_{adv} -2-1”) achieves slightly inferior results than our original SCGAN. This shows the essential role of high-quality HR face images on the guidance of learning an effective LR face restoration branch. 4) By removing three adversarial losses, the variant “ l_{adv} -3-1” performs better than the other three variants of “ l_{adv} -3-2”, “ l_{adv} -3-3”, or “ l_{adv} -3-4”. This shows that the adversarial loss in \mathcal{D}_{H2} plays a dominant role in optimizing the real-world LR face restoration branch.

4.3 Comparisons with State-of-the-art Methods

Here, we compare our SCGAN with the state-of-the-art methods on both synthetic and real-world face SR tasks. To comprehensively evaluate the performance of different methods on face SR, we perform face SR with three different degradation settings: 1) *simple* degradation with randomly bilinear or bicubic downsampling; 2) *complex* degradation with blur kernel, downsampling, synthetic noise, and JPEG compression; and 3) *real-world* unknown degradation.

Comparison methods. We compare our SCGAN with Bicubic Interpolation and other state-of-the-art methods, such as DFDNet [22], HifaceGAN [69], Real-ESRGAN [70], GFP-GAN [27], LRGAN [28], and PULSE [26]. In particular, to verify the effectiveness of our semi-cycled architecture, we also compare our SCGAN with the fully-cycled CycleGAN [32] for cycle-consistent image-to-image translation.

Face SR on simple degradation. Here, the *simple* degradation is performed by random bilinear or bicubic downsampling on the 1,000 LR face images in LS3D-W balanced dataset [63] as the test set, as described in §4.1, and we evaluate the performance of different methods on it. For a fair comparison, all the comparison methods are re-trained carefully to achieve their best results. The quantitative results of FID, KID, and LPIPS are summarized in Table 5 (2-nd row). It can be seen that our SCGAN obtains higher indices than the other competing methods. The qualitative results



Figure 7. Comparison of visual quality by our SCGAN and other face SR/real-world face SR methods on LS3D-W balanced [63] (the left part of the figure) and FFHQ [42] dataset (the right part of the figure). Please zoom in for better view.



Figure 8. Comparison of visual quality by our SCGAN and other face SR/real-world face SR methods on Widerface [63] (the left part of the figure) and WebFace dataset (the right part of the figure). Please zoom in for better view.

Table 5

Quantitative results of our SCGAN and other state-of-the-art methods on two synthetic and two real-world datasets. The best, second best, and third best results are highlighted in **red**, **blue** and **bold**, respectively.

Dataset	Metric	Bicubic Interpolation	DFDNet [22]	HifaceGAN [69]	Real-ESRGAN [70]	CycleGAN [32]	GFPGAN [27]	LRGAN [28]	PULSE [26]	SCGAN (ours)
LS3D-W balanced [63]	FID↓	274.78	277.38	238.75	57.20	51.04	51.02	33.67	33.65	22.55
	KID↓	15.31±0.11	16.60±0.11	13.56±0.12	3.08±0.07	5.81±0.11	4.45±0.11	3.95±0.10	3.49±0.16	1.26±0.06
	LPIPS↓	0.343	0.387	0.268	0.114	0.086	0.094	0.118	0.106	0.068
FFHQ [42]	FID↓	277.19	285.93	241.69	43.75	36.22	43.86	18.39	27.81	9.06
	KID↓	16.32±0.22	23.84±0.28	14.52±0.19	3.13±0.10	6.14±0.15	3.88±0.12	3.22±0.13	3.48±0.19	0.94±0.05
	LPIPS↓	0.927	0.959	0.719	0.336	0.234	0.299	0.302	0.329	0.197
Widerface [54]	FID↓	270.69	271.74	157.34	41.73	39.55	59.34	19.35	28.27	13.32
	KID↓	16.23±0.21	17.34±0.22	17.54±0.24	2.77±0.10	6.26±0.12	3.79±0.12	3.20±0.14	3.36±0.17	1.08±0.05
	NIQE↓	18.8702	7.9981	5.2294	6.7595	6.8953	6.9437	6.6446	6.7473	6.6192
WebFace	FID↓	273.96	274.49	238.10	51.57	44.94	88.71	26.49	36.02	21.06
	KID↓	18.02±0.15	19.08±0.15	14.46±0.15	3.62±0.09	6.54±0.11	6.45±0.11	4.45±0.11	3.60±0.16	1.39±0.06
	NIQE↓	7.4657	7.7320	6.0178	6.6773	6.8132	6.8841	6.4868	6.7039	6.5835

of visual quality are presented in Figure 7 (left part). One can see that DFDNet [22] and HifaceGAN [69] produce blurry results similar to those produced by Bicubic Interpolation. Real-ESRGAN, CycleGAN, and LRGAN fail to preserve well the facial structure, while PULSE and GFPGAN hard to recover well the facial details. On the contrary, our SCGAN generates realistic results in ensuring the structure and detail consistency to that of the ground-truth HR face images.

Face SR on complex degradation. Before generalizing our SCGAN to real-world face SR, we perform experiments on blind face SR with random complex degradation. Here, the complex degradation with random blur kernel, downsampling, synthetic noise, and JPEG compression is performed on the 2,500 face images in FFHQ as the test set [42], as described in §4.1. The quantitative results are listed in Table 5 (3-rd row). It can be seen that our SCGAN obtains clearly lower scores of FID, KID and LPIPS than the other methods. In Figure 7 (right part), we compare the face SR results of different methods on representative face samples in FFHQ [42]. We observe that Bicubic Interpolation, DFDNet [22] and HifaceGAN [69] still produce blurry results. Besides, Real-ESRGAN [70] and CycleGAN [32] fail to recover the face contexts. LRGAN [28] tends to produce incomplete face structure, and PULSE [26] is prone to lose the identity information or important face components like eyeglasses, while GFPGAN [27] fails to recover important face details. On the contrary, our SCGAN generates high-quality and realistic HR face images with accurate face structure and fine-grained face details. All these results validate that our SCGAN is more robust to the complex random degradation, and can produce high-quality HR face images more realistically to the real-world HR face images, than all the comparison methods.

Face SR on real-world degradation. Now we compare different methods on the Widerface [54] and our Webface dataset for real-world face SR with complex and unknown degradation, where the experimental settings are described in §4.1. The quantitative results are presented in Table 5. One can see that our SCGAN achieves higher FID and KID results than the other methods on both real-world face SR datasets. As shown in Figure 8, though achieving the best NIQE results, HifaceGAN is prone to produce very blurry face images similarly as Bicubic Interpolation, DFDNet, and Real-

Table 6

Accuracy of face detection on the SR results restored by our SCGAN and other methods on two synthetic and two real-world datasets. The best, second best, and third best results are highlighted in **red**, **blue** and **bold**, respectively.

Method	LS3D-W balanced [68]	FFHQ [42]	Widerface [54]	WebFace
Bicubic Interpolation	57.60%	48.12%	52.90%	48.05%
DFDNet [22]	41.80%	39.08%	40.55%	34.43%
HifaceGAN [69]	60.90%	63.48%	57.05%	54.28%
CycleGAN [32]	93.40%	90.44%	91.80%	89.59%
LRGAN [28]	92.60%	92.68%	93.80%	92.60%
GFPGAN [27]	96.00%	93.24%	84.55%	76.07%
SCGAN (ours)	97.80%	96.84%	96.90%	96.69%

ESRGAN. The methods of LRGAN, PULSE and GFPGAN produce either artifacts or color bias. After all, our SCGAN not only recovers the facial structure and details, but also preserves human identity of real-world LR face images, when compared to the other comparison methods.

4.4 Application on Downstream Vision Tasks

In this section, we apply our SCGAN and state-of-the-art methods to downstream vision tasks. We conduct experiment on face detection, face verification and face landmark detection in §4.4.1, §4.4.2 and §4.4.3, respectively. On all tasks, we compare our SCGAN with the methods of Bicubic Interpolation, DFDNet [22], HifaceGAN [69], CycleGAN [32], LRGAN [28], and GFPGAN [27] on face SR.

Table 7

Verification accuracy of FaceNet on the SR face images in synthetic FFHQ test set [42] restored by different methods. The best, second best, and third best results are highlighted in **red**, **blue** and **bold**, respectively.

Method	Bicubic Interpolation	DFDNet [22]	HifaceGAN [69]	CycleGAN [32]
Accuracy	22.92%	13.20%	27.00%	64.68%
Method	LRGAN [28]	GFPGAN [27]	SCGAN (ours)	Ground Truth
Accuracy	56.28%	74.56%	85.08%	97.56%

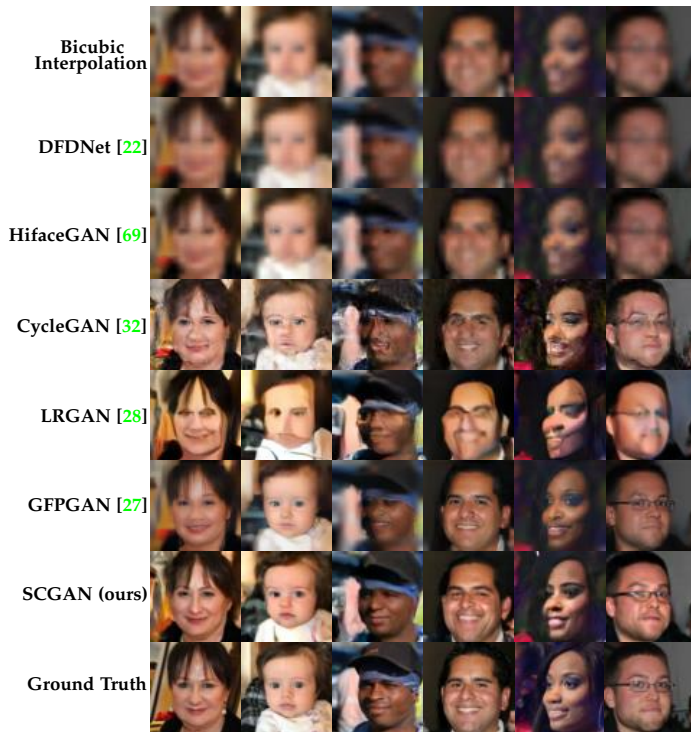


Figure 9. Comparison results of the face images restored by our SCGAN and other face SR methods on synthetic FFHQ [42] test set as introduced in §4.1. Please zoom in for better view.

4.4.1 Application on Face Detection

Face detection is to predict the bounding boxes around the faces in the images. To validate the effectiveness of these methods on face SR, we perform face detection with a simple pre-trained model of [67], which is based on Histogram of Oriented Gradient (HOG) [71] and Support Vector Machine (SVM) [72], on the SR face images by different methods. Here, we define face detection accuracy as the ratio of the number of face images successfully predicted by bounding boxes to the total number of the input face images, and each input image has exactly one face. In Table 6, we list the detection accuracies on the SR face images by different methods from the datasets of LS3D-W balanced [68], FFHQ [42], Widerface [54] and WebFace, as described in §4.1. One can see that, the simple model of “HOG+SVM” consistently achieves the highest detection accuracy on the SR face images by our SCGAN. This validates the effectiveness of our SCGAN on the face structure preservation for face detection.

4.4.2 Application on Face Verification

Face verification is a binary classification task to determine whether the pair of output and reference face images have the same identity or not. Here, we first restore the synthetic FFHQ test set [42], as introduced in §4.1, by different face SR methods. The SR face images by different methods are shown in Figure 9. One can see that the results obtained by our SCGAN maintain better the identity consistency than the other methods, when compared with the corresponding ground truths. Then we perform face verification on the restored face images by the state-of-the-art face verification method of FaceNet [73]. The accuracies of FaceNet on the SR results by different methods are listed in Table 7. It can

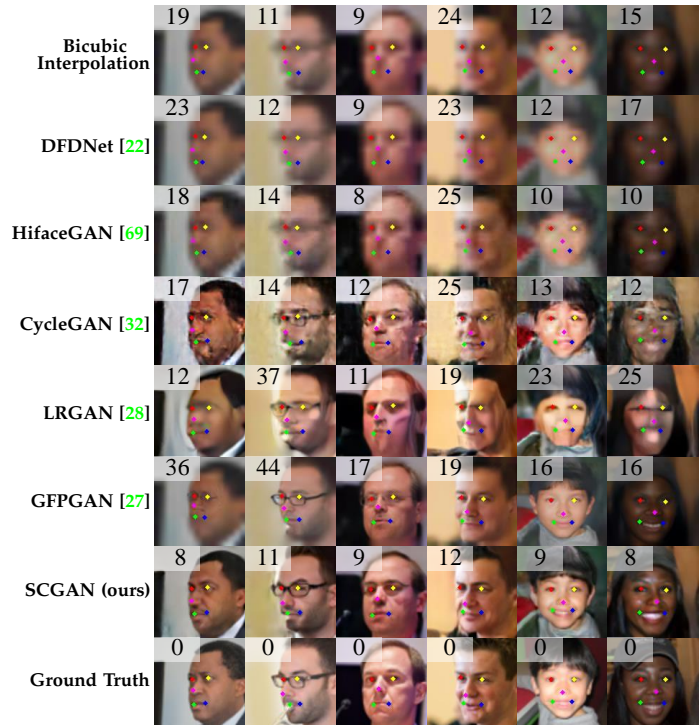


Figure 10. Comparison results of landmark detection and the corresponding ℓ_1 norm errors on the face images in synthetic FFHQ [42] dataset restored by different methods. Please zoom in for better view.

be seen that, except for the ground truths, the accuracy on the SR results of our SCGAN is clearly higher than those of the other methods. This demonstrates the superiority of our SCGAN over the other competitors on preserving the consistency of face identity information for the face SR task.

4.4.3 Application on Face Landmark Detection

Face landmark detection aims to locate the key facial components of face images. We restore the LR images into HR ones with more facial details and then use the state-of-the-art face landmark detection method of RetinaFace [74] for face landmarks detection. We compare the face SR methods on six representative LR face images degraded from FFHQ test set, as described in §4.1. The landmark detection results of six representative face images restored by different methods and the ℓ_1 norm errors (lower is better) between them and the corresponding ground truth landmarks are shown in Figure 10. We observe that, compared with the SR results of other methods, the landmarks detected by the face images restored by our SCGAN are closer to those detected on the original HR face images, and the corresponding ℓ_1 errors are also the lowest among all comparison methods. This shows that our SCGAN recovers the key facial components more detectable than the other methods for face SR.

5 CONCLUSION

In this paper, we proposed a novel Semi-Cycled Generative Adversarial Network (SCGAN) to alleviate the domain gap between unpaired LR and HR face images for real-world face super-resolution (SR). Our SCGAN contains two independent degradation branches, which are coupled by a

restoration branch, to learn the forward and backward cycle-consistent reconstruction processes. Specifically, the synthetic degradation branch learns to generate synthetic LR face images by degrading the real-world HR ones, the restoration branch aims to recover SR face images from the synthetic and real-world LR face images, and the real-world degradation branch again degrades the SR face images restored from the real-world LR ones. The restoration branch is shared and regularized by both the forward and backward cycle-consistent learning processes, making our SCGAN robust to synthetic and real-world LR face images for face SR. Experiments on two synthetic and two real-world datasets demonstrated that our SCGAN, with the proposed semi-cycled architecture, outperforms the comparison state-of-the-art methods on synthetic and real-world face SR tasks, in terms of structure preservation, detail recovery, and standard objective metrics, for real-world face SR. Three downstream vision tasks on face detection, face verification, and face landmark detection reveal that the effectiveness of our SCGAN better recovers the face structure, identity, and details than the other face SR methods.

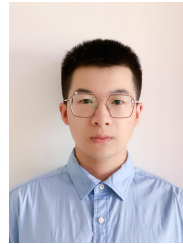
ACKNOWLEDGMENTS

This research is supported in part by The National Natural Science Foundation of China (No. 62002176, 62176068, and 61872225), Natural Science Foundation of Shandong Province (No. ZR2020MF038, ZR2020KF013, and ZR2020ZD44).

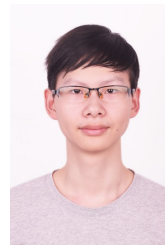
REFERENCES

- [1] B. Fasel and J. Luetttin, "Automatic facial expression analysis: a survey," *Pattern Recogn.*, vol. 36, no. 1, pp. 259–275, 2003.
- [2] W. Zhao, R. Chellappa, P. J. Phillips, and A. Rosenfeld, "Face recognition: A literature survey," *ACM computing surveys*, vol. 35, no. 4, pp. 399–458, 2003.
- [3] X. Xiong and F. De la Torre, "Supervised descent method and its applications to face alignment," in *IEEE Conf. Comput. Vis. Pattern Recog.*, 2013.
- [4] W. Liu, D. Lin, and X. Tang, "Neighbor combination and transformation for hallucinating faces," in *Int. Conf. Multimedia and Expo*, 2005.
- [5] S. W. Park and M. Savvides, "Robust super-resolution of face images by iterative compensating neighborhood relationships," in *IEEE Biometrics Symposium*, 2007.
- [6] H. Chang, D.-Y. Yeung, and Y. Xiong, "Super-resolution through neighbor embedding," in *IEEE Conf. Comput. Vis. Pattern Recog.*, vol. 1, 2004.
- [7] X. Wang and X. Tang, "Hallucinating face by eigentransformation," *IEEE Transactions on Systems, Man, and Cybernetics*, vol. 35, no. 3, pp. 425–434, 2005.
- [8] A. Chakrabarti, A. Rajagopalan, and R. Chellappa, "Super-resolution of face images using kernel pca-based prior," *IEEE Trans. Multimedia*, vol. 9, no. 4, pp. 888–892, 2007.
- [9] J.-S. Park and S.-W. Lee, "An example-based face hallucination method for single-frame, low-resolution facial images," *IEEE Trans. Image Process.*, vol. 17, no. 10, pp. 1806–1816, 2008.
- [10] Y. Hu, K. M. Lam, G. Qiu, T. Shen, and H. Tian, "Learning local pixel structure for face hallucination," in *IEEE Int. Conf. Image Process.*, 2010.
- [11] Y. Hu, K.-M. Lam, G. Qiu, and T. Shen, "From local pixel structure to global image super-resolution: A new face hallucination framework," *IEEE Trans. Image Process.*, vol. 20, no. 2, pp. 433–445, 2010.
- [12] Y. Li, C. Cai, G. Qiu, and K.-M. Lam, "Face hallucination based on sparse local-pixel structure," *Pattern Recogn.*, vol. 47, no. 3, pp. 1261–1270, 2014.
- [13] J. Shi, X. Liu, and C. Qi, "Global consistency, local sparsity and pixel correlation: A unified framework for face hallucination," *Pattern Recogn.*, vol. 47, no. 11, pp. 3520–3534, 2014.
- [14] T. Yang, P. Ren, X. Xie, and L. Zhang, "Gan prior embedded network for blind face restoration in the wild," in *IEEE Conf. Comput. Vis. Pattern Recog.*, 2021.
- [15] D. Huang and H. Liu, "Face hallucination using convolutional neural network with iterative back projection," in *Chinese Conference on Biometric Recognition*, 2016.
- [16] Y. Liu, Z. Dong, K. P. Lim, and N. Ling, "A densely connected face super-resolution network based on attention mechanism," in *IEEE Conference on Industrial Electronics and Applications*, 2020.
- [17] C. Chen, D. Gong, H. Wang, Z. Li, and K.-Y. K. Wong, "Learning spatial attention for face super-resolution," *IEEE Trans. Image Process.*, vol. 30, pp. 1219–1231, 2020.
- [18] X. Chen, X. Wang, Y. Lu, W. Li, Z. Wang, and Z. Huang, "Rbpnet: An asymptotic residual back-projection network for super-resolution of very low-resolution face image," *Neurocomputing*, vol. 376, pp. 119–127, 2020.
- [19] H. Huang, R. He, Z. Sun, and T. Tan, "Wavelet-srnet: A wavelet-based cnn for multi-scale face super resolution," in *Int. Conf. Comput. Vis.*, 2017.
- [20] X. Li, M. Liu, Y. Ye, W. Zuo, L. Lin, and R. Yang, "Learning warped guidance for blind face restoration," in *Eur. Conf. Comput. Vis.*, 2018.
- [21] B. Dogan, S. Gu, and R. Timofte, "Exemplar guided face image super-resolution without facial landmarks," in *IEEE Conf. Comput. Vis. Pattern Recog. Worksh.*, 2019.
- [22] X. Li, C. Chen, S. Zhou, X. Lin, W. Zuo, and L. Zhang, "Blind face restoration via deep multi-scale component dictionaries," in *Eur. Conf. Comput. Vis.*, 2020.
- [23] I. Goodfellow, J. Pouget-Abadie, M. Mirza, B. Xu, D. Warde-Farley, S. Ozair, A. Courville, and Y. Bengio, "Generative adversarial nets," *Adv. Neural Inform. Process. Syst.*, vol. 27, 2014.
- [24] X. Li, W. Li, D. Ren, H. Zhang, M. Wang, and W. Zuo, "Enhanced blind face restoration with multi-exemplar images and adaptive spatial feature fusion," in *IEEE Conf. Comput. Vis. Pattern Recog.*, 2020.
- [25] C. Chen, X. Li, L. Yang, X. Lin, L. Zhang, and K.-Y. K. Wong, "Progressive semantic-aware style transformation for blind face restoration," in *IEEE Conf. Comput. Vis. Pattern Recog.*, 2021.
- [26] S. Menon, A. Damian, S. Hu, N. Ravi, and C. Rudin, "Pulse: Self-supervised photo upsampling via latent space exploration of generative models," in *IEEE Conf. Comput. Vis. Pattern Recog.*, 2020.
- [27] X. Wang, Y. Li, H. Zhang, and Y. Shan, "Towards real-world blind face restoration with generative facial prior," in *IEEE Conf. Comput. Vis. Pattern Recog.*, 2021.
- [28] A. Bulat, J. Yang, and G. Tzimiropoulos, "To learn image super-resolution, use a gan to learn how to do image degradation first," in *Eur. Conf. Comput. Vis.*, 2018.
- [29] S. Maeda, "Unpaired image super-resolution using pseudo-supervision," in *IEEE Conf. Comput. Vis. Pattern Recog.*, 2020.
- [30] Y. Guo, J. Chen, J. Wang, Q. Chen, J. Cao, Z. Deng, Y. Xu, and M. Tan, "Closed-loop matters: Dual regression networks for single image super-resolution," in *IEEE Conf. Comput. Vis. Pattern Recog.*, 2020.
- [31] K. Zhang, W. Luo, Y. Zhong, L. Ma, B. Stenger, W. Liu, and H. Li, "Deblurring by realistic blurring," in *IEEE Conf. Comput. Vis. Pattern Recog.*, 2020.
- [32] J.-Y. Zhu, T. Park, P. Isola, and A. A. Efros, "Unpaired image-to-image translation using cycle-consistent adversarial networks," in *Int. Conf. Comput. Vis.*, 2017.
- [33] J. Jiang, C. Wang, X. Liu, and J. Ma, "Deep learning-based face super-resolution: A survey," *ACM Computing Surveys*, vol. 55, no. 1, pp. 1–36, 2021.
- [34] S. Baker and T. Kanade, "Hallucinating faces," in *IEEE international conference on automatic face and gesture recognition*, 2000.
- [35] B. K. Gunturk, A. U. Batur, Y. Altunbasak, M. H. Hayes, and R. M. Mersereau, "Eigenface-domain super-resolution for face recognition," *IEEE Trans. Image Process.*, vol. 12, no. 5, pp. 597–606, 2003.
- [36] Y. Zhuang, J. Zhang, and F. Wu, "Hallucinating faces: Lph super-resolution and neighbor reconstruction for residue compensation," *Pattern Recogn.*, vol. 40, no. 11, pp. 3178–3194, 2007.
- [37] T. Lu, J. Wang, J. Jiang, and Y. Zhang, "Global-local fusion network for face super-resolution," *Neurocomputing*, vol. 387, pp. 309–320, 2020.
- [38] S. Chen, Z. Han, E. Dai, X. Jia, Z. Liu, L. Xing, X. Zou, C. Xu, J. Liu, and Q. Tian, "Unsupervised image super-resolution with an

- indirect supervised path," in *IEEE Conf. Comput. Vis. Pattern Recog. Worksh.*, 2020.
- [39] X. Yu and F. Porikli, "Ultra-resolving face images by discriminative generative networks," in *Eur. Conf. Comput. Vis.*, 2016.
- [40] A. Bulat and G. Tzimiropoulos, "Super-fan: Integrated facial landmark localization and super-resolution of real-world low resolution faces in arbitrary poses with gans," in *IEEE Conf. Comput. Vis. Pattern Recog.*, 2018.
- [41] K. C. Chan, X. Wang, X. Xu, J. Gu, and C. C. Loy, "Glean: Generative latent bank for large-factor image super-resolution," in *IEEE Conf. Comput. Vis. Pattern Recog.*, 2021.
- [42] T. Karras, S. Laine, and T. Aila, "A style-based generator architecture for generative adversarial networks," in *IEEE Conf. Comput. Vis. Pattern Recog.*, 2019.
- [43] X. Chen, Y. Duan, R. Houthoofd, J. Schulman, I. Sutskever, and P. Abbeel, "Infogan: Interpretable representation learning by information maximizing generative adversarial nets," *Adv. Neural Inform. Process. Syst.*, vol. 29, 2016.
- [44] M. Mirza and S. Osindero, "Conditional generative adversarial nets," *arXiv preprint arXiv:1411.1784*, 2014.
- [45] P. Isola, J.-Y. Zhu, T. Zhou, and A. A. Efros, "Image-to-image translation with conditional adversarial networks," in *IEEE Conf. Comput. Vis. Pattern Recog.*, 2017.
- [46] T.-C. Wang, M.-Y. Liu, J.-Y. Zhu, A. Tao, J. Kautz, and B. Catanzaro, "High-resolution image synthesis and semantic manipulation with conditional gans," in *IEEE Conf. Comput. Vis. Pattern Recog.*, 2018.
- [47] Z. Yi, H. Zhang, P. Tan, and M. Gong, "Dualgan: Unsupervised dual learning for image-to-image translation," in *Int. Conf. Comput. Vis.*, 2017.
- [48] T. Kim, M. Cha, H. Kim, J. K. Lee, and J. Kim, "Learning to discover cross-domain relations with generative adversarial networks," in *Int. Conf. Mach. Learn.*, 2017.
- [49] R. Yi, Y.-J. Liu, Y.-K. Lai, and P. Rosin, "Quality metric guided portrait line drawing generation from unpaired training data," *IEEE Trans. Pattern Anal. Mach. Intell.*, 2022.
- [50] C. Szegedy, V. Vanhoucke, S. Ioffe, J. Shlens, and Z. Wojna, "Rethinking the inception architecture for computer vision," in *IEEE Conf. Comput. Vis. Pattern Recog.*, 2016.
- [51] G. Hinton, O. Vinyals, J. Dean *et al.*, "Distilling the knowledge in a neural network," *Adv. Neural Inform. Process. Syst.*, vol. 27, 2014.
- [52] K. He, X. Zhang, S. Ren, and J. Sun, "Deep residual learning for image recognition," in *IEEE Conf. Comput. Vis. Pattern Recog.*, 2016.
- [53] L. Van der Maaten and G. Hinton, "Visualizing data using t-sne." *Journal of machine learning research*, vol. 9, no. 11, pp. 2579–2605, 2008.
- [54] S. Yang, P. Luo, C.-C. Loy, and X. Tang, "Wider face: A face detection benchmark," in *IEEE Conf. Comput. Vis. Pattern Recog.*, 2016.
- [55] M. Heusel, H. Ramsauer, T. Unterthiner, B. Nessler, and S. Hochreiter, "Gans trained by a two time-scale update rule converge to a local nash equilibrium," *Adv. Neural Inform. Process. Syst.*, vol. 30, 2017.
- [56] Z. Wang, A. C. Bovik, H. R. Sheikh, and E. P. Simoncelli, "Image quality assessment: from error visibility to structural similarity," *IEEE Trans. Image Process.*, vol. 13, no. 4, pp. 600–612, 2004.
- [57] G. B. Huang, M. Mattar, T. Berg, and E. Learned-Miller, "Labeled faces in the wild: A database for studying face recognition in unconstrained environments," in *Workshop on faces in 'Real-Life' Images: detection, alignment, and recognition*, 2008.
- [58] T. Miyato, T. Kataoka, M. Koyama, and Y. Yoshida, "Spectral normalization for generative adversarial networks," in *Int. Conf. Learn. Represent.*, 2018.
- [59] G. Xu, J. Xu, Z. Li, L. Wang, X. Sun, and M. Cheng, "Temporal modulation network for controllable space-time video super-resolution," in *IEEE Conf. Comput. Vis. Pattern Recog.*, 2021.
- [60] K. He, X. Zhang, S. Ren, and J. Sun, "Delving deep into rectifiers: Surpassing human-level performance on imagenet classification," in *Int. Conf. Comput. Vis.*, 2015.
- [61] D. Kingma and J. Ba, "Adam: A method for stochastic optimization," in *Int. Conf. Learn. Represent.*, 2015.
- [62] A. Paszke, S. Gross, F. Massa, A. Lerer, J. Bradbury, G. Chanan, T. Killeen, Z. Lin, N. Gimelshein, L. Antiga *et al.*, "Pytorch: An imperative style, high-performance deep learning library," *Adv. Neural Inform. Process. Syst.*, vol. 32, 2019.
- [63] A. Bulat and G. Tzimiropoulos, "How far are we from solving the 2d & 3d face alignment problem?(and a dataset of 230,000 3d facial landmarks)," in *Int. Conf. Comput. Vis.*, 2017.
- [64] M. Bińkowski, D. J. Sutherland, M. Arbel, and A. Gretton, "Demystifying mmd gans," in *Int. Conf. Learn. Represent.*, 2018.
- [65] R. Zhang, P. Isola, A. A. Efros, E. Shechtman, and O. Wang, "The unreasonable effectiveness of deep features as a perceptual metric," in *IEEE Conf. Comput. Vis. Pattern Recog.*, 2018.
- [66] A. Mittal, R. Soundararajan, and A. C. Bovik, "Making a "completely blind" image quality analyzer," *IEEE Signal Process. Let.*, vol. 20, no. 3, pp. 209–212, 2012.
- [67] Q. Zhu, M.-C. Yeh, K.-T. Cheng, and S. Avidan, "Fast human detection using a cascade of histograms of oriented gradients," in *IEEE Conf. Comput. Vis. Pattern Recog.*, 2006.
- [68] A. Bulat and G. Tzimiropoulos, "How far are we from solving the 2D & 3D face alignment problem? (and a dataset of 230,000 3D facial landmarks)," in *Int. Conf. Comput. Vis.*, 2017.
- [69] L. Yang, S. Wang, S. Ma, W. Gao, C. Liu, P. Wang, and P. Ren, "Hifacegan: Face renovation via collaborative suppression and replenishment," in *ACM Int. Conf. Multimedia*, 2020.
- [70] X. Wang, L. Xie, C. Dong, and Y. Shan, "Real-esrgan: Training real-world blind super-resolution with pure synthetic data," in *Int. Conf. Comput. Vis.*, 2021.
- [71] N. Dalal and B. Triggs, "Histograms of oriented gradients for human detection," in *IEEE Conf. Comput. Vis. Pattern Recog.*, 2005.
- [72] C. J. Burges, "A tutorial on support vector machines for pattern recognition," *Data mining and knowledge discovery*, vol. 2, no. 2, pp. 121–167, 1998.
- [73] F. Schroff, D. Kalenichenko, and J. Philbin, "Facenet: A unified embedding for face recognition and clustering," in *IEEE Conf. Comput. Vis. Pattern Recog.*, 2015.
- [74] J. Deng, J. Guo, E. Ververas, I. Kotsia, and S. Zafeiriou, "Retinaface: Single-shot multi-level face localisation in the wild," in *IEEE Conf. Comput. Vis. Pattern Recog.*, 2020.



Hao Hou received his B.Sc. degree in Information and Computing Science from the School of Mathematical Science, University of Jinan in 2019. He is currently an M.Sc. student with the College of Intelligence and Information Engineering, Shandong University of Traditional Chinese Medicine, Ji'nan, China. His current research interests are in the areas of image processing, medical image processing and analysis.



Xiaotao Hu received his B.Sc. degree in School of Software Engineering, Dalian University of Technology in 2021. He is currently an M.Sc. student with the College of Computer Science, Nankai University, Tianjin, China. His current research interests are in the areas of image processing, medical image processing and analysis.



Jun Xu received his B.Sc. and M.Sc. degrees from School of Mathematics Science, Nankai University, Tianjin, China, in 2011 and 2014, respectively, and the Ph.D. degree from the Department of Computing, Hong Kong Polytechnic University, in 2018. He worked as a Research Scientist at IIAI, Abu Dhabi, UAE. He is currently an Associate Professor with School of Statistics and Data Science, Nankai University. More information can be found at <https://csjunxu.github.io/>.



Yingkun Hou received his Ph.D. degree from the School of Computer Science and Technology, Nanjing University of Science and Technology in 2012. He is currently an associate professor with the School of Information Science and Technology, Taishan University, Taian, China. His current research interests are in the areas of image processing, pattern recognition, and artificial intelligence.



Benzheng Wei received the B.S. degree in computer science from School of Computer Science at Shandong Institute of Light Industry, Jinan, China, in 2000, the M.S. degree in computer science from School of Computer Science and Technology at Shandong University, Jinan, China, in 2007, and the Ph.D. degree in precision instrument and machinery from College of Automation Engineering at Nanjing University of Aeronautics and Astronautics, Nanjing, China, in 2013. He is a professor with Shandong University of Traditional

Chinese Medicine. He is also acting as a director at both the Center for Medical Artificial Intelligence and the Computational Medicine Lab of Shandong University of Traditional Chinese Medicine. His current research interests are in artificial intelligence, medical information engineering and computational medicine. He has published over 80 papers in refereed international leading journals/conferences such as Medical Image Analysis, IEEE TMI, Neurocomputing, IPMI and MICCAI.



Dinggang Shen received the Ph.D. degree in electrical engineering from Shanghai Jiao Tong University, Shanghai, China, in 1995. He has published more than 1100 peer-reviewed papers in the international journals and conference proceedings, with H-index 120. His research interests include medical image analysis, computer vision, and pattern recognition. Dr. Shen served on the Board of Directors, the Medical Image Computing and Computer Assisted Intervention (MICCAI) Society, in 2012–2015, and was the

General Chair for MICCAI 2019. He is a fellow serves as an editorial board member for eight international journals. He is a Fellow of the American Institute for Medical and Biological Engineering and the International Association for Pattern Recognition. He is currently the founding dean of the School of Biomedical Engineering, ShanghaiTech University, Shanghai, China.